Lissajous fiber scanning for forward viewing optical endomicroscopy using asymmetric stiffness modulation

Hyeon-Cheol Park, Yeong-Hyeon Seo, and Ki-Hun Jeong*

Department of Bio and Brain Engineering and KAIST Institute for Optical Science and Technology, Korea Advanced Institute of Science and Technology, 291 Daehak-ro, Yuseong-gu, Daejeon 305-701, South Korea
kjeong@kaist.ac.kr

Abstract: We report a fully packaged and compact forward viewing endomicroscope by using a resonant fiber scanner with two dimensional Lissajous trajectories. The fiber scanner comprises a single mode fiber with additional microstructures mounted inside a piezoelectric tube with quartered electrodes. The mechanical cross-coupling between the transverse axes of a resonant fiber with a circular cross-section was completely eliminated by asymmetrically modulating the stiffness of the fiber cantilever with silicon microstructures and an off-set fiber fragment. The Lissajous fiber scanner was fully packaged as endomicroscopic catheter passing through the accessory channel of a clinical endoscope and combined with spectral domain optical coherence tomography (SD-OCT). *Ex-vivo* 3D OCT images were successfully reconstructed along Lissajous trajectory. The preview imaging capability of the Lissajous scanning enables rapid 3D imaging with high temporal resolution. This endoscopic catheter provides many opportunities for on-demand and non-invasive optical biopsy inside a gastrointestinal endoscope.

OCIS codes: (170.4500) Optical coherence tomography; (170.2150) Endoscopic imaging; (170.3880) Medical and biological imaging; (120.5800) Scanners.

References and links

1. D. Provenzale and J. Onken, "Surveillance issues in inflammatory bowel disease: ulcerative colitis," J. Clin. Gastroenterol. **32**(2), 99–105 (2001).
2. B. J. Reid, P. L. Blount, Z. Feng, and D. S. Levine, "Optimizing endoscopic biopsy detection of early cancers in Barrett's high-grade dysplasia," Am. J. Gastroenterol. **95**(11), 3089–3096 (2000).
3. D. S. Levine, R. C. Haggitt, P. L. Blount, P. S. Rabinovitch, V. W. Rusch, and B. J. Reid, "An endoscopic biopsy protocol can differentiate high-grade dysplasia from early adenocarcinoma in Barrett's esophagus," Gastroenterology **105**(1), 40–50 (1993).
4. B. J. Reid, W. M. Weinstein, K. J. Lewin, R. C. Haggitt, G. VanDeventer, L. DenBesten, and C. E. Rubin, "Endoscopic biopsy can detect high-grade dysplasia or early adenocarcinoma in Barrett's esophagus without grossly recognizable neoplastic lesions," Gastroenterology **94**(1), 81–90 (1988).
5. J. B. Pawley, *Handbook of Biological Confocal Microscopy,* 2nd ed. (Plenum Press, 1995).
6. W. Denk, J. H. Strickler, and W. W. Webb, "Two-photon laser scanning fluorescence microscopy," Science **248**(4951), 73–76 (1990).
7. D. Huang, E. A. Swanson, C. P. Lin, J. S. Schuman, W. G. Stinson, W. Chang, M. R. Hee, T. Flotte, K. Gregory, C. A. Puliafito, and J. G. Fujimoto, "Optical coherence tomography," Science **254**(5035), 1178–1181 (1991).
8. T. D. Wang and J. Van Dam, "Optical biopsy: A new frontier in endoscopic detection and diagnosis," Clin. Gastroenterol. Hepatol. **2**(9), 744–753 (2004).
9. W. Piyawattanametha, R. P. J. Barretto, T. H. Ko, B. A. Flusberg, E. D. Cocker, H. Ra, D. Lee, O. Solgaard, and M. J. Schnitzer, "Fast-scanning two-photon fluorescence imaging based on a microelectromechanical systems two- dimensional scanning mirror," Opt. Lett. **31**(13), 2018–2020 (2006).
10. W. Jung, D. T. McCormick, Y.-C. Ahn, A. Sepehr, M. Brenner, B. Wong, N. C. Tien, and Z. Chen, "In vivo three-dimensional spectral domain endoscopic optical coherence tomography using a microelectromechanical system mirror," Opt. Lett. **32**(22), 3239–3241 (2007).
11. A. D. Aguirre, P. R. Hertz, Y. Chen, J. G. Fujimoto, W. Piyawattanametha, L. Fan, and M. C. Wu, "Two-axis MEMS Scanning Catheter for Ultrahigh Resolution Three-dimensional and En Face Imaging," Opt. Express **15**(5), 2445–2453 (2007).

#204833 - $15.00 USD Received 15 Jan 2014; revised 24 Feb 2014; accepted 24 Feb 2014; published 5 Mar 2014

12. K. H. Kim, B. H. Park, G. N. Maguluri, T. W. Lee, F. J. Rogomentich, M. G. Bancu, B. E. Bouma, J. F. de Boer, and J. J. Bernstein, "Two-axis magnetically-driven MEMS scanning catheter for endoscopic high-speed optical coherence tomography," Opt. Express **15**(26), 18130–18140 (2007).
13. W. Jung, S. Tang, D. T. McCormic, T. Xie, Y.-C. Ahn, J. Su, I. V. Tomov, T. B. Krasieva, B. J. Tromberg, and Z. Chen, "Miniaturized probe based on a microelectromechanical system mirror for multiphoton microscopy," Opt. Lett. **33**(12), 1324–1326 (2008).
14. M. J. Gora, J. S. Sauk, R. W. Carruth, K. A. Gallagher, M. J. Suter, N. S. Nishioka, L. E. Kava, M. Rosenberg, B. E. Bouma, and G. J. Tearney, "Tethered capsule endomicroscopy enables less invasive imaging of gastrointestinal tract microstructure," Nat. Med. **19**(2), 238–240 (2013).
15. D. C. Adler, Y. Chen, R. Huber, J. Schmitt, J. Connolly, and J. G. Fujimoto, "Three-dimensional endomicroscopy using optical coherence tomography," Nat. Photonics **1**(12), 709–716 (2007).
16. P. H. Tran, D. S. Mukai, M. Brenner, and Z. Chen, "In vivo endoscopic optical coherence tomography by use of a rotational microelectromechanical system probe," Opt. Lett. **29**(11), 1236–1238 (2004).
17. J.-M. Yang, C. Favazza, R. Chen, J. Yao, X. Cai, K. Maslov, Q. Zhou, K. K. Shung, and L. V. Wang, "Simultaneous functional photoacoustic and ultrasonic endoscopy of internal organs in vivo," Nat. Med. **18**(8), 1297–1302 (2012).
18. T. Xie, H. Xie, G. K. Fedder, and Y. Pan, "Endoscopic Optical Coherence Tomography with a Modified Microelectromechanical Systems Mirror for Detection of Bladder Cancers," Appl. Opt. **42**(31), 6422–6426 (2003).
19. W. Piyawattanametha, H. Ra, Z. Qiu, S. Friedland, J. T. C. Liu, K. Loewke, G. S. Kino, O. Solgaard, T. D. Wang, M. J. Mandella, and C. H. Contag, "In vivo near-infrared dual-axis confocal microendoscopy in the human lower gastrointestinal tract," J. Biomed. Opt. **17**(2), 021102 (2012).
20. H.-C. Park, C. Song, M. Kang, Y. Jeong, and K.-H. Jeong, "Forward imaging OCT endoscopic catheter based on MEMS lens scanning," Opt. Lett. **37**(13), 2673–2675 (2012).
21. J. Wu, M. Conry, C. Gu, F. Wang, Z. Yaqoob, and C. Yang, "Paired-angle-rotation scanning optical coherence tomography forward-imaging probe," Opt. Lett. **31**(9), 1265–1267 (2006).
22. F. Helmchen, M. S. Fee, D. W. Tank, and W. Denk, "A Miniature Head-Mounted Two-Photon Microscope. High-Resolution Brain Imaging in Freely Moving Animals," Neuron **31**(6), 903–912 (2001).
23. B. A. Flusberg, J. C. Jung, E. D. Cocker, E. P. Anderson, and M. J. Schnitzer, "In vivo brain imaging using a portable 3.9 gram two-photon fluorescence microendoscope," Opt. Lett. **30**(17), 2272–2274 (2005).
24. D. R. Rivera, C. M. Brown, D. G. Ouzounov, I. Pavlova, D. Kobat, W. W. Webb, and C. Xu, "Compact and flexible raster scanning multiphoton endoscope capable of imaging unstained tissue," Proc. Natl. Acad. Sci. U.S.A. **108**(43), 17598–17603 (2011).
25. T. Wu, Z. Ding, K. Wang, M. Chen, and C. Wang, "Two-dimensional scanning realized by an asymmetry fiber cantilever driven by single piezo bender actuator for optical coherence tomography," Opt. Express **17**(16), 13819–13829 (2009).
26. X. Liu, M. J. Cobb, Y. Chen, M. B. Kimmey, and X. Li, "Rapid-scanning forward-imaging miniature endoscope for real-time optical coherence tomography," Opt. Lett. **29**(15), 1763–1765 (2004).
27. E. J. Seibel, R. S. Johnston, and C. D. Melville, "A full-color scanning fiber endoscope," in Optical Fibers and Sensors for Medical Diagnostics and Treatment Applications VI(San Jose, CA, 2006), pp. 608303–608308.
28. M. T. Myaing, D. J. MacDonald, and X. Li, "Fiber-optic scanning two-photon fluorescence endoscope," Opt. Lett. **31**(8), 1076–1078 (2006).
29. C. J. Engelbrecht, R. S. Johnston, E. J. Seibel, and F. Helmchen, "Ultra-compact fiber-optic two-photon microscope for functional fluorescence imaging in vivo," Opt. Express **16**(8), 5556–5564 (2008).
30. L. Huo, J. Xi, Y. Wu, and X. Li, "Forward-viewing resonant fiber-optic scanning endoscope of appropriate scanning speed for 3D OCT imaging," Opt. Express **18**(14), 14375–14384 (2010).
31. Y. Zhang, M. L. Akins, K. Murari, J. Xi, M.-J. Li, K. Luby-Phelps, M. Mahendroo, and X. Li, "A compact fiber-optic SHG scanning endomicroscope and its application to visualize cervical remodeling during pregnancy," Proc. Natl. Acad. Sci. U.S.A. **109**(32), 12878–12883 (2012).
32. J. Xi, Y. Chen, Y. Zhang, K. Murari, M.-J. Li, and X. Li, "Integrated multimodal endomicroscopy platform for simultaneous en face optical coherence and two-photon fluorescence imaging," Opt. Lett. **37**(3), 362–364 (2012).
33. S. Moon, S.-W. Lee, M. Rubinstein, B. J. F. Wong, and Z. Chen, "Semi-resonant operation of a fiber-cantilever piezotube scanner for stable optical coherence tomography endoscope imaging," Opt. Express **18**(20), 21183–21197 (2010).
34. W. Liang, K. Murari, Y. Zhang, Y. Chen, M.-J. Li, and X. Li, "Increased illumination uniformity and reduced photodamage offered by the Lissajous scanning in fiber-optic two-photon endomicroscopy," J. Biomed. Opt. **17**(2), 021108 (2012).
35. O. M. El Rifai and K. Youcef-Toumi, "Coupling in piezoelectric tube scanners used in scanning probe microscopes," in *Proceedings of the 2001 American Control Conference. (Cat. No.01CH37148)* (IEEE, 2001), **5**, 3251–3255.
36. C. L. Hoy, N. J. Durr, and A. Ben-Yakar, "Fast-updating and nonrepeating Lissajous image reconstruction method for capturing increased dynamic information," Appl. Opt. **50**(16), 2376–2382 (2011).
37. J. T. C. Liu, M. J. Mandella, N. O. Loewke, H. Haeberle, H. Ra, W. Piyawattanametha, O. Solgaard, G. S. Kino, and C. H. Contag, "Micromirror-scanned dual-axis confocal microscope utilizing a gradient-index relay lens for image guidance during brain surgery," J. Biomed. Opt. **15**(2), 026029 (2010).
38. T. Tuma, J. Lygeros, V. Kartik, A. Sebastian, and A. Pantazi, "High-speed multiresolution scanning probe microscopy based on Lissajous scan trajectories," Nanotechnology **23**(18), 185501 (2012).

#204833 - $15.00 USD Received 15 Jan 2014; revised 24 Feb 2014; accepted 24 Feb 2014; published 5 Mar 2014

39. H.-C. Park, C. Song, and K.-H. Jeong, "Micromachined lens microstages for two-dimensional forward optical scanning," Opt. Express **18**(15), 16133–16138 (2010).

1. Introduction

Optical endomicroscopy has raised a great deal of attention for in-vivo clinical applications such as optical biopsy or imaging guided surgery. Current medical endoscopy simply observes a reflected optical image from mucosal surface and it often requires physical biopsies, i.e., resection of some suspicious tissues from a patient body for *ex-vivo* histological or cytological examination. The main drawback of current endoscopic biopsy is unavailability of on-demand and real-time clinical diagnosis. In other words, microscopic examination after tissue resection not only causes significant time delay for clinical decision but also it may fail to predict tumor-free resection margin [1–4]. On the other hand, recent development of optical imaging techniques such as confocal microscopy, multi-photon microscopy, and optical coherence tomography (OCT) visualizes the depth of tumor invasion from mucosal resection of intact tissues or organs from characteristic optical signatures with microscopic resolution [5–7]. The miniaturization of advanced imaging systems and further implementation inside an clinical endoscope can provide new directions for *in-vivo* optical biopsy [8].

The optical integration inside an endomicroscope is challenging and still under development due to the strict spatial and operational restrictions as well as a lack of small optical components. Recently, micro-electro-mechanical systems (MEMS) offer unique solutions for endomicroscopic integration with real-time and electrically safe operations. For example, side-viewing endomicroscopes have been extensively initiated by scanning MEMS mirrors [9–13]. Circumferential viewing for tubular organs or vasculatures has also been realized by rotating a fiber-prism assembly with an external rotator [14, 15] or internal micro-motors [16, 17]. On the other hand, forward-viewing endomicroscope is very essential for some particular applications such as gastroscopic diagnosis and becomes of great interest since it can be immediately applicable through the accessory channel of conventional endoscopes. Scanning MEMS mirror based forward optical scanning occupies relatively large space over the clear aperture due to an additional mirror [18, 19]. Other schemes such as MEMS lens scanning [20], paired-lens rotation [21], and scanning optical fiber [22–34] can secure the maximum clear aperture within the confined package. In particular a scanning optical fiber coupled to piezo-bender actuators [22–25] or a tubular piezoelectric (PZT) actuator with quartered electrodes [26–34], has many attractive figures-of-merits such as compact, simple, and robust packaging, where two-dimensional laser scanning with affordable scan amplitudes can still be achieved by operating at resonance in order to amplify the scanning amplitude at low operational voltages. Spiral scanning by using amplitude modulated sinusoidal driving waveforms with identical frequencies has been mainly used for these resonant fiber scanners [27–32], while the Lissajous scanning has also been implemented by selecting slightly different resonant frequencies within a resonance bandwidth [33, 34]. However, an eccentricity of a PZT tube due to inevitable machining tolerance or a slight misalignment between a circular fiber and a PZT often causes considerable cross-coupling between the transverse scanning axes [35]. This mechanical coupling between transverse scan axes substantially broadens the line scan width, which not only deteriorates the image resolution but also increases complexity of scanning control.

Here we report a resonant fiber scanner with 2D Lissajous trajectories for forward viewing 3D OCT endomicroscopy by asymmetric stiffness modulation. The fiber scanner comprises a single mode fiber implemented inside a piezoelectric tube with quartered electrodes and additional microstructures (Fig. 1(a)). The additional structures include both extra masses at the distal end of a scanning fiber and an off-set fiber fragment with micromachined silicon structures. This additional mass not only shortens the fiber length for a compact packaging with the resonant frequencies below the detection speed of the SD-OCT system but also enables low voltage operations due to high mechanical quality factor (Q-factor). Besides, the off-set fiber fragment with micromachined silicon structures substantially reduces the cross-coupling effect due to the separation of resonant frequencies along the transverse axes by

#204833 - $15.00 USD Received 15 Jan 2014; revised 24 Feb 2014; accepted 24 Feb 2014; published 5 Mar 2014

differentiating mechanical stiffness. Depending on the ratio of scanning frequencies, the decouple motion finally enables Lissajous scanning, which covers a rectangular image area with high density grid-like pattern. The Lissajous scanning can provide many attractive figure-of-merits for miniaturized laser scanning based imaging systems such as endomicroscopes. First, sufficient scanning amplitude can be achieved within electrical safety limit by the resonant operation of both axes. Second, it provides more illumination uniformity than that of the spiral scanning and can avoid photodamage due to the high illumination density at the center region of the spiral scanning [34]. Finally, the Lissajous scanning provides the fast preview of an entire image area over the scan time, where the transverse resolution continuously increased (Fig. 1(b)) until the scan completes the 2D trajectory. Unlike non-resonant raster scanning with high operation power of non-resonant scanning, or the resonant spiral scanning, this unique feature of Lissajous scanning serves as an attractive method for miniaturized laser scanning based imaging systems such as endomicroscopes [36–38].

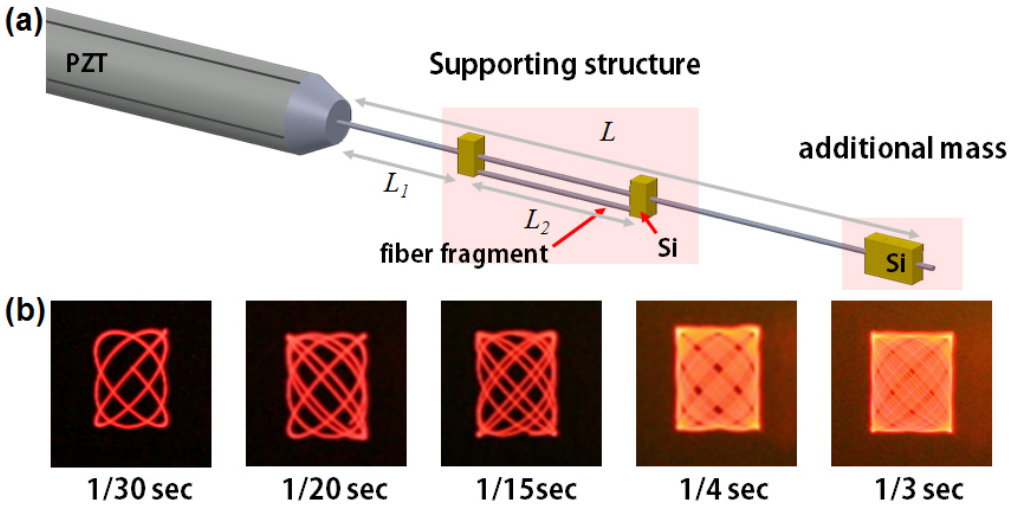

Fig. 1. (a) Schematic illustration of a Lissajous fiber scanner mounted inside a quardrapole piezoelectic tube with micromachined silicon structures. (b) Time-lapse sequence of Lissajous scanning patterns. The mechanical stiffness of a scanning fiber with a circular cross-section is tuned by mounting additional microstuctures along the off-axis, which results in Lissajous scan trajectories due to the separation of resonant frequencies along transverse axes. The scan density during Lissajous scanning continuously increases and covers the entire field of view.

2. Fabrication and characterizations of a Lissajous fiber scanner

A Lissajous pattern fiber scanner was assembled with a single-mode optical fiber, silicon microstructures, a fiber fragment, and a PZT tubular actuator (2.2 mm in diameter and 20 mm in length). The silicon microstructures were micromachined by using deep reactive ion etching (DRIE) on a 500 μm thick heavily doped 6-inch silicon wafer with good electrical conductivity. Figure 2(a) illustrates the microfabrication procedures for silicon microstructures. First, the back-side of a silicon wafer was deposited with a thin aluminum layer to not only improve heat conduction but also prevent leakages of helium cooling gas during a DRIE process. The top silicon layer was patterned with photoresist and defined on the whole wafer by using DRIE. Finally, the remained photoresist and aluminum layer were completely removed by using plasma ashing and aluminum wet etching. Figure 2(b) and 2(c) show the optical images of micromachined silicon structures. Each silicon structure has a physical dimension of 0.5 x 0.5 x 1 mm^3 with a rectangular shape, where a fiber groove was defined at the center of a single silicon microstructure for precise microassembly. Y-shaped silicon tethers with 10 μm in width were also used to maintain the mechanical connection

#204833 - $15.00 USD Received 15 Jan 2014; revised 24 Feb 2014; accepted 24 Feb 2014; published 5 Mar 2014

between silicon wafer and microstructures during the microfabrication as shown in Fig. 2(c). The individual silicon microstructures were finally separated from the wafer by disconnecting silicon tethers with Joule heating [39]. Note that MEMS microfabrication techniques enable to fabricate diverse shapes of silicon microstructures, which can be utilized for modulating or enhancing the scanning properties of a resonant fiber scanner with high precision and low cost.

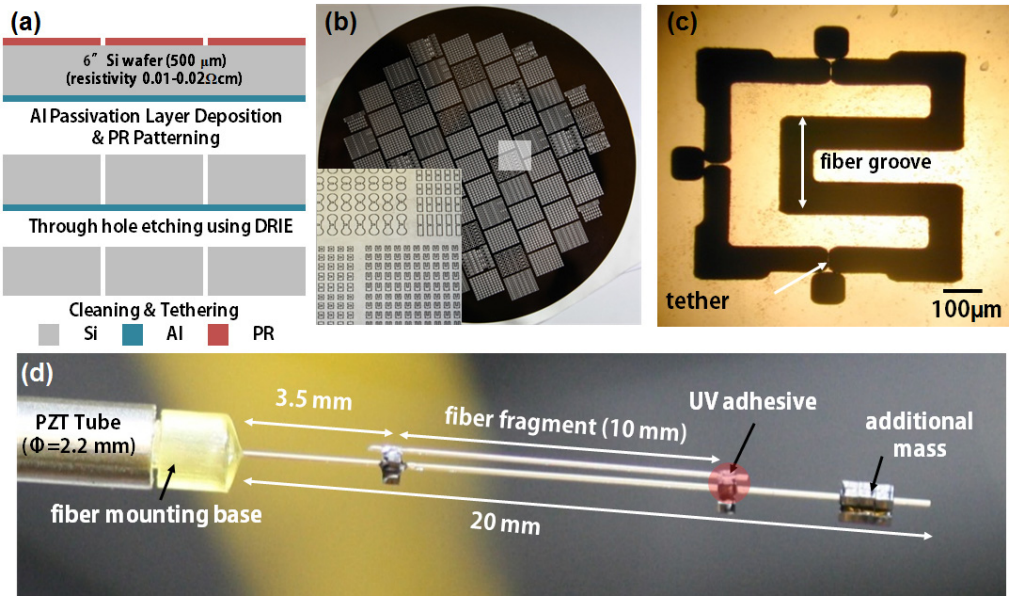

Fig. 2. Lissajous fiber scanner; (a) Microfabrication method for supporting silicon structures. The silicon structures were fabricated by using conventional DRIE process with 6 inch silicon wafer. (b) Optical images of a micromachined silicon substrate; silicon microstructures can be arbitrarily shaped by using MEMS microfabrication techniques. (c) An optical image of a single silicon microstructure; the fiber groove was defined on a silicon structure to assist the precise assembly. The individual silicon structures were tethered on a silicon wafer and separated by breaking them with Joule heating. (d) An optical image of fully micro-assembled Lissajous fiber scanner. A 20 mm long fiber cantilever with additional supporting structures was mounted on a PZT tube.

The microassembly of a Lissajous fiber scanner started with a 20 mm long fiber cantilever mounted inside a tubular PZT actuator. Two mounting heads made of an engineering plastic were used at the front and back of a PZT tube for precise alignment along the optical axis. Three silicon microstructures were firstly attached at the distal end of a single mode fiber as an additional mass. Two additional silicon microstructures were positioned at 3.5 mm and 13.5 mm of the optical fiber apart from the PZT actuator, where a fiber fragment was glued on the fiber grooves of silicon microstructures with UV curable epoxy. The orientation of silicon microstructures was precisely aligned with the electrodes of the PZT tube. An additional fiber fragment of 10 mm in length was finally attached at the bottom side of silicon structures by considering the motion orientation of PZT actuators. Figure 2(d) shows an optical image of a fully assembled Lissajous fiber scanner.

#204833 - $15.00 USD Received 15 Jan 2014; revised 24 Feb 2014; accepted 24 Feb 2014; published 5 Mar 2014

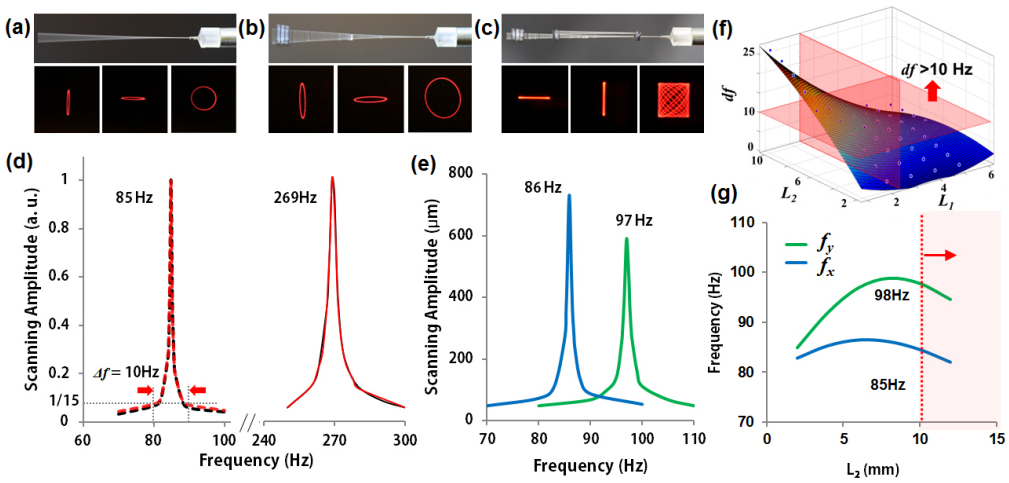

Fig. 3. (a)-(c) Optical images of resonant scanning fiber cantilevers and biaxial scan patterns; (a) 20 mm long bare fiber cantilever, (b) fiber cantilever with three additional masses, (c) fiber cantilever with additional supporting structures. Bottom three images are corresponds to the 1D resonant scan patterns of *x*-axis (left), *y*-axis (center), and 2D scan pattern (right), respectively. Ellipsoidal scan patterns were observed due to the mechanical cross-coupling (a) and became more significant due to the high resonance gain induced by additional mass (b). The cross-coupling phenomena were completely eliminated with additional supporting structure, which enables to obtain clear line scan patterns and Lissajous scanning (c). (d)-(e) Frequency response of resonant fiber scanner. A 20 mm long fiber cantilever with a circular cross-section originally has the resonance at 269 Hz for both *x* and *y* directions. With three additional silicon masses at the distal end of a fiber, the resonant frequency was decreased to 85 Hz, while the mechanical Q-factor increases. The resonance bandwidth, which a resonance gain reduced to 1/15, was 10 Hz (indicated with red arrow). (e) Frequency response of the resonant fiber scanner with additional supporting structure. The supporting structure distinguishes the resonance frequencies of both axes; 86 Hz for *x*-axis, and 97 Hz for *y*-axis, respectively. Scanning amplitude of 732 μm and 591.7 μm for *x* and *y* axes, respectively, were obtained with peak-to-peak 40 V_{ac} applied voltages. (e) A second-order regression model for the resonant frequency difference between two orthogonal axes of the 20 mm long fiber cantilever, with respect to the position of additional structures, L_1, and length, L_2. The mechanical dimensions of the supporting structure were carefully selected regarding on the numerical analysis within above horizontal red plane area (*df* >10 Hz), for sufficiently separating the resonant frequencies of orthogonal axes to eliminate the mechanical cross-coupling. (f) The resonant frequency of each axis under a constant L_1 of 3.5 mm depending on L_2. The stiffness of a fiber fragment decreases as the fragment length L_2 increases over 10 mm.

Figure 3 demonstrates the scanning properties of Lissajous fiber scanners. A fiber cantilever with 20 mm in length shows the same resonant frequencies at 269 Hz for both *x* and *y* directions, respectively. An ellipsoidal scan pattern during one axis operation is observed due to mechanical cross-coupling between both the axes (Fig. 3(a)). Additional micromachined silicon mass, precisely mounted at the distal end of the fiber cantilever, decreases the resonant frequencies while increasing the mechanical Q-factor. In other words, three silicon masses not only decrease the resonant frequency from 269 Hz to 85 Hz, which is below the detection speed of the SD-OCT system (~100Hz) but also increase Q-factor from 55 to 105 (Fig. 3(d)), which increases the scan amplitudes. In contrast, high Q-factor not only makes the fiber scanner vulnerable to environmental perturbations and complicated to control [33] but also it increases the resonance gain for the other axis, resulting in substantial mechanical cross-coupling (Fig. 3(b)). However, an additional fiber fragment effectively eliminates the cross-coupling between the transverse axes and thus provides clear line-scan patterns (Fig. 3(c)), where the resonant frequencies along the fast and slow scanning axes are separated by more than the resonance bandwidth, i.e., 86 Hz and 97 Hz for *x* and *y* directions, respectively (Fig. 3(e)). The deflection transfer functions were 18.3μm/V and 14.8μm/V that the scanning amplitude of 732 μm and 591.7 μm for *x*-axis and *y*-axis, respectively, were obtained within the electrical safety limit of peak-to-peak 40 V_{ac} applied voltages. The

#204833 - $15.00 USD Received 15 Jan 2014; revised 24 Feb 2014; accepted 24 Feb 2014; published 5 Mar 2014

decouple motion of Lissajous fiber scanners was also numerically analyzed with a second-order regression model (Fig. 3(f)). The numerical results clearly indicate that the frequency separation substantially depends on both the position L_1 and the length L_2 of a fiber fragment. For this particular experiment, the cross-coupling ratio, i.e., the scan amplitude ratio of x-axis to y-axis, is 15 pixels/256 pixels. From this numerical analysis model, the frequency separation at resonance was set to be above 10 Hz, corresponding to the resonance bandwidth (red arrow in Fig. 3(d)), where the resonance gain is reduced by less than 1/15 for the decoupled motion. Figure 3(g) shows the resonant frequencies depending on L_2 under a constant L_1 of 3.5 mm. The stiffness of a fiber fragment decreases as the fragment length L_2 increases by above 10 mm, which no longer follows the regression model.

3. Lissajous scanning 3D OCT imaging with endomicroscope

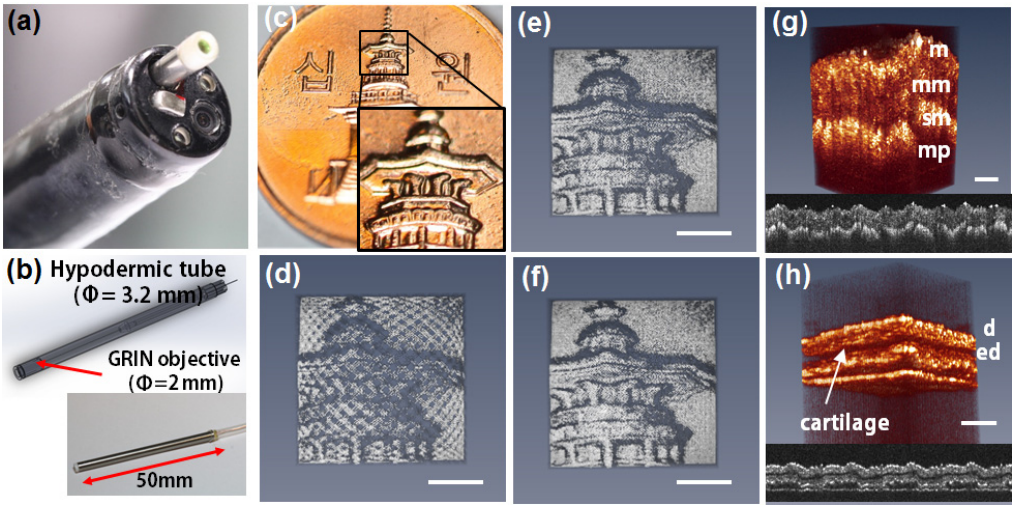

Fig. 4. (a) Fully packaged OCT endomicroscope inside a gastrointestinal endoscope. The endomicroscope with compact packaging passes through the accessory channel. (b) Schematic and optical image of forward viewing OCT endomicroscopic catheter. (c) Optical image of a national coin. (d)-(f) time-lapse reconstructed 3D OCT image of the national coin with the detection time of 1 sec (d), 1.5 sec (e) and 2 sec (f). (g)-(h) Ex-vivo OCT images of porcine colon (g) and mouse ear (h). 2D cross-sectional OCT images with 3000 consecutive points along the Lissajous trajectories (subset) were assigned on a specific location of the detection volume and reconstructed to a 3D image (256 x 256 x 995 voxels); mucosa (m), muscularis mucosa (mm), submucosa (sm), and muscularis propria (mp), dermis (d), epidermis (ed). Scale bar; 1 mm.

The fiber scanner was fully assembled with a hypodermic tube housing of 3.2 mm in diameter and a gradient index (GRIN) of 2 mm in diameter and 5 mm in length. The GRIN objective lens was positioned at 0.25 mm apart from the fiber distal end, providing a ~4.95x magnification with an 8.3 mm working distance. The spot size at a focal plane was measured to 34 μm, which is fairly consistent with fiber mode field diameter of 5.6 μm while a small expands in spot size is due to the machining tolerance of the housing and misalignment during the assembly. The endomicroscopic catheter has 50 mm in full length. Figure 4(b) shows a schematic illustration and an optical image of the fully packaged endoscopic catheter, which can pass through the accessory channel of clinical endoscopes for future clinical applications such as image guided surgery or optical biopsies (Fig. 4(a)).

Lissajous scan based 3D OCT imaging was successfully demonstrated with the endomicroscope coupled with high-speed SD-OCT system (60 kHz A-line scan rate) and direct 3D volume mapping based on non-repeating Lissajous patterns, which was described in our previous work [20]. The SD-OCT system consists of a broadband light source of 830 nm center wavelength (Exalos, $\Delta\lambda$ = 46.8 nm, Max. Power 4.99 mW), 2 x 2 fiber coupler, and a

#204833 - $15.00 USD Received 15 Jan 2014; revised 24 Feb 2014; accepted 24 Feb 2014; published 5 Mar 2014

home-built spectrometer with a 2048 pixels CMOS line scan camera (Basler, spL 2048–140 km). The axial resolution of the system was measured to 7 μm, while the bandwidth of the light source determines the theoretical value of 6.49 μm in air. For a 3D imaging, the resonant frequencies of the Lissajous fiber scanner was fairly adjusted within a resonance bandwidth so that a pattern densely covering the whole field-of-view (FOV). Then, while the Lissajous fiber scanner was resonantly scanned, a series of consecutive A-line data sets along the Lissajous trajectory and control signals of the PZT tube were simultaneously obtained from a DAQ board and a CMOS line scan camera, respectively. Finally, each measured interference spectra was directly assigned to a corresponding pixel on a detection volume by using measured driving signals. Note that, the imaging sequence is not based on a fixed Lissajous pattern that repeats with a particular rate, but the sampling density of the scan patterns can be continuously adjusted by increasing the detection time. Lissajous scanned OCT image for a national coin (Fig. 4(c)) with complex en-face inscription was firstly obtained for the validation of the 3D reconstruction algorithm. Figure 4(d)-(f) shows the time-lapse sequence of fully reconstructed OCT images. The Lissajous scan trajectories initially fill with coarse density across the full FOV and then densely samples the OCT signals over time. The sampling density reaches up to 38% in 1 sec with 60k A-line data sets (Fig. 4(d)), consecutively up to 59% and 69% within 1.5 and 2 seconds, respectively (Fig. 4(e) and (f); 90k and 120k A-line data sets, respectively). The Lissajous scan enables the rapid recognition of an entire texture within FOV within 1 sec (Fig. 4(d)) and further samples sequentially contribute to the improvement of transverse resolution by filling up the sampling gap as long as the minimum feature size of a sample target is smaller than the sampling gaps (Fig. 4(e), (f)). This unique preview imaging capability of the Lissajous scanning can remarkably reduce detection time and can be effectively utilized for fast volumetric imaging, especially in case of exploring suspicious regions within a large FOV or the temporal resolution is much important. *Ex-vivo* histological analysis with the fabricated endomicroscopy was also achieved. Figure 4(g) and (h) shows the reconstructed volumetric OCT images of porcine colon and mouse ear with 256 x 256 x 995 voxels. The images were captured within only 0.5 second, and the 3 x 3 mm^2 FOV images were reconstructed with 30k A-line data sets (The 1st 3k consecutive points along the Lissajous trajectories are shown in subset image), while the detail layer structures underneath the tissue surface were readily identified.

4. Conclusion

To conclude, we have successfully demonstrated a forward-viewing OCT endomicroscope based on the Lissajous fiber scanner. The cross-coupling of conventional resonant fiber scanners were completely eliminated by decoupling the scanning resonant frequencies along the transverse axes with additional supporting silicon structures with an off-set fiber fragment. Microfabrication capability offers the diverse shapes of silicon microstructures, which can be further utilized for modulating the scanning properties. Lissajous scanning also allows rapid and accurate 3D SD-OCT imaging. This Lissajous pattern fiber scanner can provide many opportunities for advanced forward viewing endomicroscopic imaging based on confocal microscopy, multi-photon microscopy, or other laser scanning based imaging modalities. Moreover, this endoscopic catheter can be directly applicable through the accessory channel of a conventional gastrointestinal endoscope and it can also realize new directions for on-demand, rapid, and non-invasive endoscopic optical biopsy.

Acknowledgments

This work was financially supported Samsung Advanced Institute of Technology (SAIT), and Global Frontier Project (CISS-2012M3A6A6054199), Basic Science Research Program through the National Foundation of Korea (NRF) funded by the Ministry of Science, ICT & Future Planning (MSIP 2013035236), and Korean Health Technology R&D Project, Ministry of Health & Welfare, South Korea (HI13C2181).